Construction and Building Materials 281 (2021) 122574

Contents lists available at ScienceDirect

Construction and Building Materials

journal homepage: www.elsevier.com/locate/conbuildmat

The effects of nanosilica on the fresh and hardened properties of 3D printable mortars

Pawel Sikora [a,b], Sang-Yeop Chung [c,*], Maxime Liard [d], Didier Lootens [d], Tobias Dorn [a], Paul H. Kamm [e], Dietmar Stephan [a], Mohamed Abd Elrahman [a,f]

[a] Building Materials and Construction Chemistry, Technische Universität Berlin, Germany
[b] Faculty of Civil and Environmental Engineering, West Pomeranian University of Technology Szczecin, Poland
[c] Department of Civil and Environmental Engineering, Sejong University, Seoul, South Korea
[d] Sika Technology AG – Central Research, Zurich, Switzerland
[e] Institute of Applied Materials, Helmholtz Centre Berlin, Berlin, Germany
[f] Structural Engineering Department, Mansoura University, Mansoura, Egypt

HIGHLIGHTS

- 3D printable mortars containing different dosages of nanosilica (NS) were developed and evaluated.
- NS accelerates significantly the setting and hardening of printable mortar, while reducing its open time.
- Increment of yield stress, together with an increment in NS dosage, was found to have occurred.
- Optimal NS dosage results in improvement of the compressive strength and pore structure.
- Incorporation of NS in the mixture resulted in improved buildability and decrement in pore anisotropy.

ARTICLE INFO

Article history:
Received 21 May 2020
Received in revised form 7 December 2020
Accepted 30 January 2021

Keywords:
3D printing
Mortar
Nanosilica
Micro-CT
Hydration
Fresh properties
Hardened properties

ABSTRACT

This study presents the experimental results of an investigation on the effects of nanosilica (NS) on the material characteristics of printable mortars used for additive manufacturing. Printable cement mortars based on Ordinary Portland Cement, limestone filler and silica sand were modified with different dosages of nanosilica (from 2% to 6% by weight of binder) and its influence on their hydration, rheological, mechanical and transport properties was assessed. The study showed that NS accelerates significantly the setting and hardening of printable mortar, while reducing its open time. Moreover, an increment of yield stress, together with an increment in NS dosage, was found to have occurred. The incorporation of an optimal NS dosage results in a noticeable increase in the compressive strength and alteration of the pore structure as determined by the MIP measurements. Moreover, transport properties of the produced mortar are significantly improved due to incorporation of NS. In addition to the microstructure refinement, Micro-CT and scanning electron microscopy (SEM) studies revealed that 3D printed mortars exhibit pore anisotropy in accordance with the printing direction. However, incorporation of NS in the mixture resulted in improved buildability, thus decreasing pore anisotropy.

1. Introduction

Additive manufacturing (AM), also referred to as 3D printing, is a method of constructing a structure via a layer-by-layer process. It is one of the most successful emerging fields in civil engineering and one of the key pillars of the Industry 4.0 concept [1]. This interest owes to new structural possibilities, which cannot be achieved with a conventional construction process [2]. In conventional concrete construction projects, the majority of the total cost is spent on formwork and labor [3,4], but since formwork is not required in 3D printing and because project times are short due to the continuous work of the printer, a dramatic reduction in project costs can be achieved [5]. Moreover, this technology offers unprecedented geometrical freedom, enabling the creation of advanced architectural structures. To date, numerous comprehensive review papers have described the potential of 3D printing in

* Corresponding author at: Department of Civil and Environmental Engineering, Sejong University, 209 Neungdong-ro, Gwangjin-gu, Seoul 05006, South Korea.
E-mail address: sychung@sejong.ac.kr (S.-Y. Chung).

https://doi.org/10.1016/j.conbuildmat.2021.122574
0950-0618/

concrete technology, including descriptions of printing methods, material composition, as well as cost and environmental analyses [1,3,4,6–9].

Although concrete printing technology has seen spectacular development in the industry, there is still room to develop further improved properties of 3D printing material [10]. As has been reported, the microstructure of 3D printed concrete differs noticeably from that of conventional concrete [11] and due to the specifics of the printing process and a lack of local vibration heterogeneity, void formation between subsequent layers of materials and cold joints may occur [8,11–13]. In addition, the introduction of a high amount of fines, along with a low w/c ratio, results in the presence of an increased amount of unreacted material in the matrix [6,11,13]. Van der Putten et al. [12] have reported that 3D printed concrete possesses many flat and elongated pores, especially in the inter-layer transition zone. Similarly, Lee et al. [14] have reported slightly increased porosity in the inter-layer zones of 3D printed specimens, although they did not find pore volume to be directly correlated with the tensile strength of specimens. However, Keita et al. [15] reported that that drying as well as time gap between successive deposition of layers has a major impact on the interface strength of printable composites.

Various admixtures are used to produce printable concrete with satisfying pumpability, extrudability, buildability as well as fast setting [16–20]. Recently, significant attention has been paid to nanomaterials, which due to their high reactivity (attributable to their ultrafine size and high specific surface area), exhibit unique physical properties as well as significant chemical reactivity [21,22]. As such, even a small dosage has a substantial effect on both the fresh and hardened properties of cementitious composites. To date, nanomaterials have mainly been incorporated in 3D printing technology as thixotropy modifying admixtures [22–24]. Van den Heever et al. [25] have reported that the addition of 2% (by weight of cement, bwoc) of silicon carbide (SiC) nanoparticles significantly improves the printability of concrete, by enhancing its thixotropy and increasing inter-layer bond strength. However, a slight retardation in early strength development was also reported. Zhu et al. [26] have incorporated attapulgite nanoclay (ANC), in the amount of 0.5% bwoc, as an admixture which improves thixotropy in 3D printable, ultra-high tensile ductile engineered cementitious composites. The study showed a beneficial effect on the printability of such composites when ANC was added to the mixture. Zhang et al. [27] have performed a comparative study of the effects of NC and silica fume (SF) admixtures, showing that both can enhance the thixotropy and buildability of 3D printed concrete, with a higher rate of increase corresponding to the use of NC (as compared to silica fume). Similarly, other researchers [28] have reported that even a low dosage of NC (0.1% bwoc) increases suspension viscosity and flocculation, which in turn improves structural stability and leads to better extrusion and a longer open time. Despite the beneficial effects of NC on the buildability of 3D printed concrete, some authors have reported that NC-incorporated concretes exhibit higher amounts of macropores in the interfacial bond, as compared to pristine concrete, as a result of their noticeably increased thixotropy [13]. Cho et al. [29] have reported that nanosilica (NS), due to its high SSA, can be another suitable material for optimizing the rheological properties of a printable mixture. Their study showed that NS in the amount of 2 wt-% improves the buildability of lightweight foamed printable concrete. Besides enhancing its fresh properties, the same authors have also reported [30] that the incorporation of NS in a mixture results in a more refined and denser cement matrix structure and thus a higher mechanical strength. Mendoza Reales et al.'s [8] comprehensive and comparative study on the effects of nanosilica, microsilica, metakaolin and nanoclay as potential structural buildup agents for printable cement pastes, has shown that NS, followed by NC, is the most effective thickening admixture. NS is more efficient than NC in modifying rheological properties normalized per solid substitution.

Although there has been some success in incorporating nanoparticles in printable cementitious materials, as mentioned above, most of the available research has been limited to a characterization of rheological properties, with less attention paid to hardened composite properties; particularly microstructure or durability related properties. This study aims to fill this gap in the literature and to present an investigation of the material characteristics of nanosilica-modified mortar compositions used in the 3D printing process. Accordingly, the hydration, rheological, mechanical and transport properties of printable mortars were analyzed. In addition, to assess the pore characteristics of the 3D printed mortar, a comprehensive microstructural analysis utilizing micro-computed tomography (micro-CT), mercury intrusion porosimetry (MIP) and scanning electron microscopy (SEM) was also performed.

2. Materials and mixture design

2.1. Materials

The printable mortars used in this study were composed of Ordinary Portland Cement (OPC) CEM I 52.5 N, two limestone fillers: fine (d50 = 2 μm) and coarse (d50 = 46 μm) and fine crushed silica sand with an aggregate size of 0.2–1 mm and a mean value of about 0.4 mm. Particle size distribution of used materials are given in Fig. 1.

A polycarboxylate ether-based (PCE) superplasticizer (SP) was used in order to facilitate mixing and to reduce water demand of mortar. Moreover, a fixed amount of thickening agent (xanthan gum), 0.09% by weight of binder, was added to prevent any segregation of the mortar and to improve its printability. To conform with EN-1008, tap water was used for all mixes.

2.2. Nanosilica

The NS used in this study was a commercially available suspension of colloidal silica (density of 1.4 g/cm^3, pH = 9.5, and solid content of 50 wt-%). High-resolution transmission electron microscope (TEM) micrographs confirmed that the NS particles were spherical (Fig. 2a-b). The particle size, according to TEM (Fig. 2c), was determined by the computer software to be between 10 nm and 140 nm. X-ray diffraction (XRD) patterns (Fig. 2d) confirmed its high purity and amorphicity. The properties of nanostructures have been comprehensively described in our previous work [31].

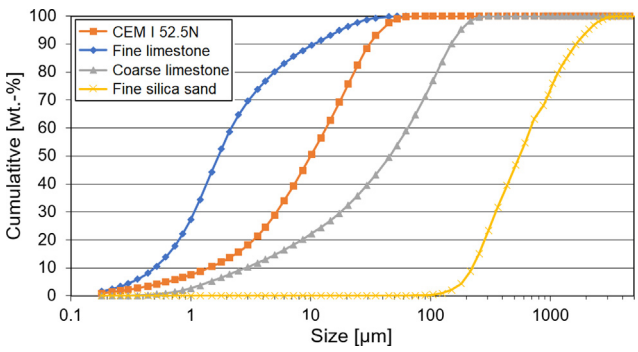

Fig. 1. Particle size distribution of mortar constituents.

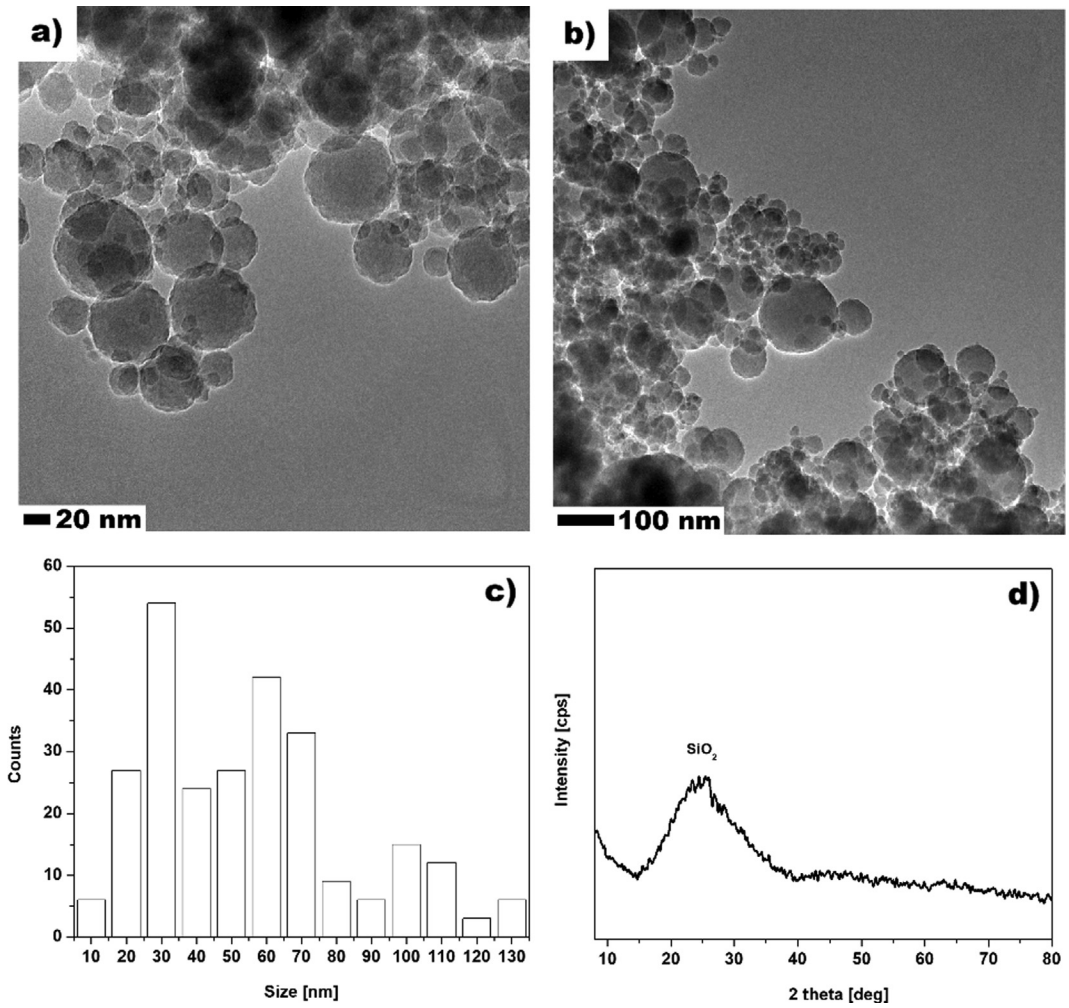

Fig. 2. TEM images (a-b), size distribution (c), XRD (d) of NS. . Reproduced from [31]

2.3. Mixture compositions and the printing process

The mixture compositions of the printable mortars are presented in Table 1. In all mixtures, the ratios of solid mortar components remained fixed. Mortars were modified with different dosages of nanosilica (from 2% to 6% by weight of binder). Moreover, due to incorporation of NS to the mixture slight increment of SP content was required. The SP content in mortars was adapted to achieve the comparable consistency of the printable mortar. Similar to other studies [32–34] the consistency was determined using a flow-table method (conforming EN 1015–3) with targeted flow between 140 and 155 mm. In all the mixtures tested, the water-to-solid ratio was set to 0.14, which corresponds to a water-to-cement ratio of w/c = 0.52. During the addition of NS, the amount of tap water was reduced to take into account the water present in the NS solution.

A 5 L planetary mixer was used to prepare the mixture. The dry components were first placed in a bucket and then mixed with nanosilica (if used) and superplasticizer, prior to the addition of water. After the addition of the water, the components were mixed; firstly for 120 s at 140 rpm and then for another 180 s at 240 rpm.

The printer used in this study was a customized version of the Delta WASP 2040 (WASP, Italy). It was modified to enable the 3D printing of mortar, with the previously mixed mortar poured into an extruder and pumped through a 10 mm diameter tube toward the printer. The nozzle used for all tests had a diameter of 6 mm. The printing speed was 10 mm/s and the average layer thickness

Table 1
Ratio of components in printable mortar mixtures.

Mix	Cement	Fine limestone powder	Coarse limestone powder	Silica sand	Water	SP* [%]	Thickening agent* [%]	NS* [%]
0NS	1	0.3	0.5	1.8	0.52	0.24	0.09	–
2NS	1	0.3	0.5	1.8	0.52	0.24	0.09	2
3NS	1	0.3	0.5	1.8	0.52	0.24	0.09	3
4NS	1	0.3	0.5	1.8	0.52	0.27	0.09	4
6NS	1	0.3	0.5	1.8	0.52	0.28	0.09	6

*Percentage by weight of binder.

in printed element was 2 mm. A set of cuboid elements (40·40·40 mm^3) were printed for the evaluation of microstructural properties with the size for effective micro-CT measurements. Fig. 3a represents a 3D model made with CAD software, which was used to create the 3D printer (Fig. 3b) readable G-code file. The printed object is also represented in this picture, being a perfect reconstruction of the piece designed (Fig. 3c). To evaluate the compressive strength of the specimens two types of specimens were prepared. First series of specimens were printed into 40·40·160 mm^3 prisms based on the printing path described in work of Hirsch et al. [35] (Fig. 4). To produce second series of specimens (casted) the nozzle was lifted and mortar was poured into the molds. Afterwards, specimen was vibrated.

3. Methods

3.1. Isothermal calorimetry and in-situ XRD

The hydration study of the binder phase of the printable mortar was assessed using two techniques. The first, calorimetry measurement, was performed using an isothermal conduction calorimeter (MC-CAL/100P, C3 Prozess- und Analysetechnik). The second, an in-situ X-ray diffraction (XRD) measurement, was performed using an XRD EMPYREAN, PANalytical. Only the binder phase (excluding the aggregate fraction) of the printable mortar was used to track hydration kinetics. Due to an increased binder phase water demand, as well as because of the need to facilitate the accurate specimen preparation required for the measuring process, the SP content was increased to 1 wt-%. The binder, water, SP and NS (if used) were mixed for 1 min in a dedicated plastic container and, immediately after mixing, the hydration heat of the samples was measured for up to 7 d. In order to perform the in-situ XRD measurement, the samples were poured into steel molds with 7 cm^2 surfaces and a depth of 2 mm. The molds containing the samples were in direct contact with the temperature-controlled sample stage, which was set to 20 °C. To protect the samples from surface drying and atmospheric CO_2, they were covered with a Kapton film of 7.5 μm thickness, during the entire measurement procedure.

3.2. Rheological measurements

An MCR 301 (Anton Paar) stress imposed rheometer, equipped with calibrated helicoidal geometry [36,37] and specially designed for cementitious materials, was used [38] to carry out the rheological measurement of the printable mortar. The outer geometry surface is rough [39] to reduce the wall slip effect [40]. The following procedure was applied: (i) pre-shearing for 10 s at a constant shear-rate of 100 s^{-1}, (ii) determination of shear-stress as a function of shear-rate, from 100 s^{-1} to 0.1 s^{-1}, with 30 points distributed evenly along a logarithmic scale, for a total of 300 s. Particular effort was made to ensure that air was not entrapped during the rheological tests, since this is known to significantly affect rheological measurements [41].

3.3. Setting time and strength evolution

To determine the strength evolution and setting time of the printable mortars ultrasonic wave reflection method was applied. Measurement was performed using a compact 8-cell, custom-built, ultrasonic device containing three ultrasonic shear wave transducers bonded to one waveguide per cell (Fig. 5). The device was used to measure the reflection loss coefficient of a reflected wave generated at the interface of a waveguide and a hydrating cement-based composite. Afterwards, the shear modulus of the specimen is estimated from this measurement, which is related to the elastic modulus and, ultimately, the compressive strength. In addition, based on the obtained data the initial and final setting time of cementitious composite can be determined. Therefore, this non-invasive technique enables continuous compressive strength tracking of the specimen from the first minutes of hydration process. The full details of the device and measuring technique have been presented in [42,43].

After the mixing process, the printable mortars were poured directly into the cells, aligned and covered with plastic foil, so as to avoid water evaporation. Each measurement was performed for up to 10 h with three repetitions, with the mean values taken as being representative.

3.4. Penetration measurement test

This technique allows measurement of the evolution of the force needed to push a conically shaped needle (radius 3 mm and length 8 mm) into a sample, placed in a pot (Fig. 5). Needle penetration speed was constant throughout the experiment, with the force recorded evolving as the structure formed. It was thus possible to measure the force evolution from a few seconds after mixing, up to the initial setting time. Furthermore, using the needle dimensions, it is possible to convert the force needed to push in the needle, into the compressive strength of the penetrated material [43].

3.5. Compressive strength determination

Compressive strength after 7 and 28 d of curing were determined on 40·40·160 mm^3 printed and casted mortars. A modern digital crushing machine (Toni Technik, Berlin, Germany), conforming to EN 196–1, was used for compressive strength determination. Six specimens of each type of mortar mix were tested, with the mean value taken into consideration.

3.6. Transport properties

The water accessible porosity of the printable mortars was determined using the water displacement method. After 28 d of curing, the saturated mass (m_{sat}) of the specimens was determined, along with the saturated mass of specimens underwater (m_{uw}). The samples were then dried at 105 °C to a constant mass and weighed

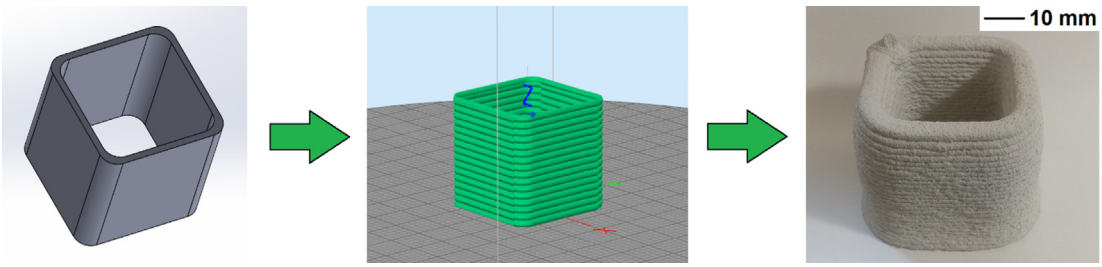

Fig. 3. 3D model (a), slicing (b), printed element (c) used for micro-CT evaluations.

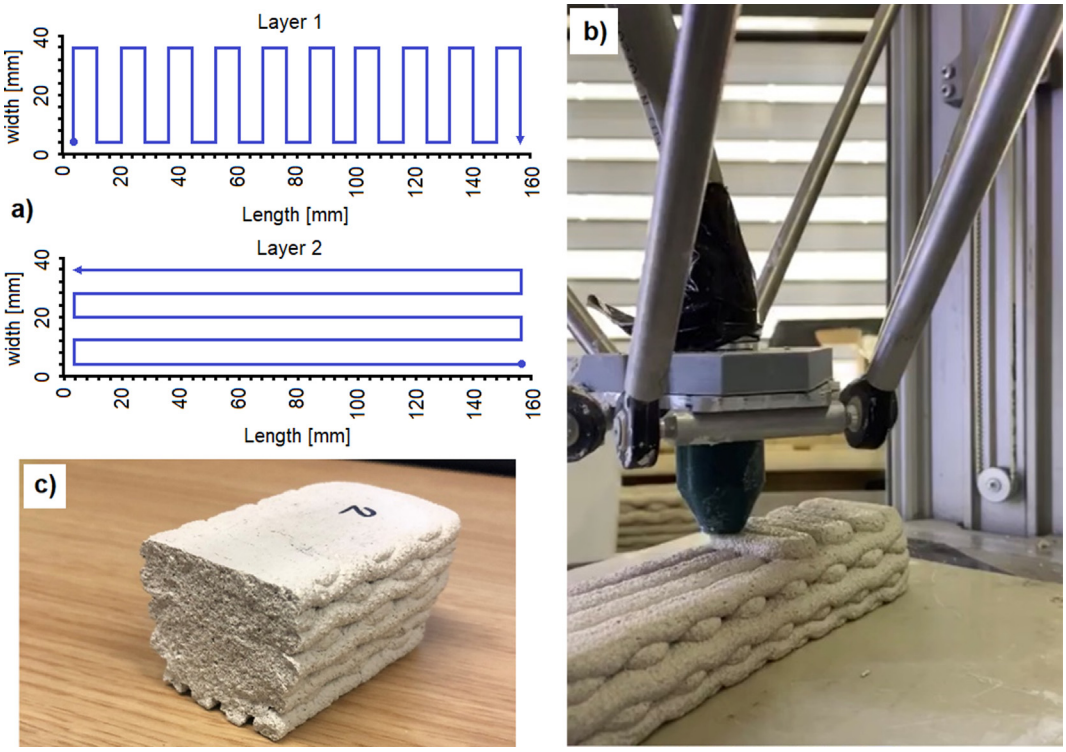

Fig. 4. Printing path of first two layers of a prism (a), specimen during printing (b), printed element used for compressive strength evaluations (c).

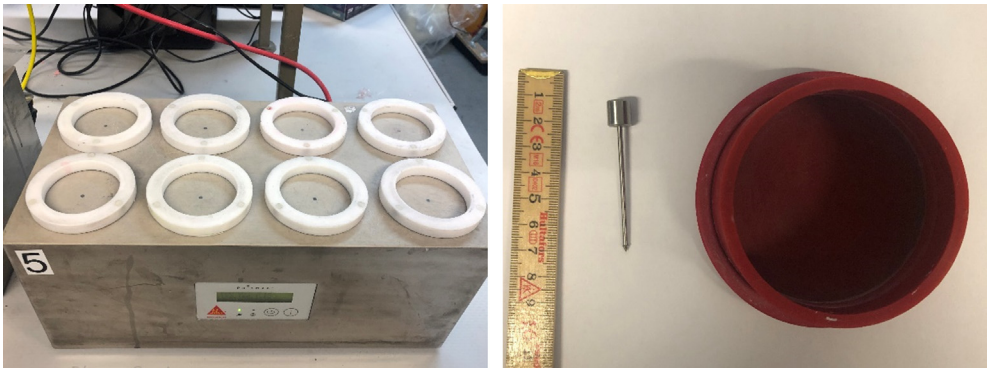

Fig. 5. Ultrasonic testing device (left) and penetrometer geometry (right).

(m_{dry}). Finally, the water accessible porosity was determined by applying Eq. (1). Three specimens of each type of mortar mix were tested, with the mean value being taken into consideration.

$$P = \frac{m_{sat} - m_{dry}}{m_{sat} - m_{uw}} \times 100 \ [\%] \quad (1)$$

The water absorption coefficient of the cement mortars was determined using the partial immersion method, following the guidelines of EN ISO 15148. Three specimens of each type of mortar mix were tested, with the mean value being taken into consideration. Prior to measurement, the sides of the specimens were coated with paraffin wax to ensure one-directional water flow in the mortars. The specimens were weighed at selected time intervals to characterize their water uptake. Based on the sorptivity curve, the water absorption coefficient was then calculated as the ratio between the mass of water absorbed by the specimen, per area of suction, and the square root of time.

3.7. Oven-dry density and thermal conductivity

The oven-dry densities of the mortar specimens were measured after 28 d of curing, in accordance with EN 12390–7. Three samples of each case were oven-dried at 105 °C until reaching a constant mass, with the mean value being selected as the dry density. The specimens were then used to determine thermal conductivity, using the transient plane source method (Hot Disk, Göteborg, Sweden), conforming to ISO 22007–2. Two samples were used for each test, with the Hot Disk sensor positioned between the samples. The test was repeated three times on different samples from each mix, with the mean value taken into consideration.

3.8. Mercury intrusion porosimetry (MIP)

Mercury intrusion porosimetry (MIP) was utilized to obtain information about the pore size distribution in the printable mortar matrix. This method is effective for assessing the pore structure of cementitious composites with a wide range of pore diameters

[31,44,45]. After 28 d of curing, small-cored samples were drilled out from the middle of the printed specimens and immersed immediately in isopropanol to stop hydration. They were subsequently freeze-dried prior to testing. The intrudable pore volume of the hardened samples was determined using a Pascal 140 and 240 series (Thermo Scientific) mercury intrusion porosimeter. The mercury density was 13.5450 g/mL, the surface tension was taken as 0.48 N/m, while the selected contact angle was 140°.

3.9. Micro-computed tomography (micro-CT)

The microstructural characteristics of the printable mortar specimens were also evaluated using X-ray micro-computed tomography (micro-CT). Micro-CT can provide the geometrical characteristics of materials both in 2D and 3D; this approach is a very supportive technique which, combined with MIP, enables the enhancement of the measurement range of pore characteristics [46–49].

Fig. 6 shows the micro-CT imaging procedure. Since the printed specimen had an irregular shape, a region of interest (ROI) was selected from it; its cross-sectional image was visualized, as shown in the 4th image of Fig. 6. In this study, the cross-sectional images along the *z*-axis, which is the direction of height, were composed of 500·500 pixels with a 30.0 μm pixel size; a total of 1000 images were stacked to construct the 3D image. As shown in Fig. 6, most parts of the specimens were selected as the ROI, and the selected region can be considered as the RVE (representative volume element) of the printed specimen. Image segmentation was used to classify specific phases of the specimen, such as pores. Otsu's thresholding method [50] and manual adjustment were used to select a proper threshold, with the image segmentation and construction performed using the imaging toolbox in MATLAB (R2019b) [51]. In the 2D and 3D binary images (image 6 of Fig. 6), the white represents pores within the specimen.

Probability functions, such as two-point correlation [52,53] and lineal-path functions [54,55], were also used to examine pore characteristics, particularly the anisotropy of the pores. With these functions, probabilistic characteristics such as relative pore clustering, can be examined using two random points (two-point correlation function, P_2) or a test line (lineal path function, L_2). Detailed descriptions of these functions can be found in [53,55], with only a general formulation presented here, as follows:

$$\lim_{r\to 0} P_2(r,\theta,\varnothing) = f_v, \lim_{r\to\infty} P_2(r,\theta,\varnothing) = [f_v]^2 \quad (1)$$

$$\lim_{r\to 0} L_2(r,\theta,\varnothing) = f_v, \lim_{r\to\infty} L_2(r,\theta,\varnothing) = 0 \quad (2)$$

In the equations above, r is the distance between the two points, θ is the angle between the test line and the z-axis, $\varnothing$ is the angle between the projection of the test line on the xy-plane and f_v is the volume fraction of pores. The solid characteristics of the specimens were also examined using micro-CT images, since pixel values are determined according to the relative density of solid structures.

3.10. Scanning electron microscopy (SEM) analysis

Low-vacuum scanning electron microscope, (SEM, Zeiss GeminiSEM500 NanoVP) was used to support the MIP and micro-CT evaluations discussed above. 3D printed specimens were cut into slices along the sample height and then polished. Prior to this, measurement specimens were dried in a freeze-dryer.

4. Results and discussion

4.1. Isothermal calorimetry

Fig. 7 represents the results of binder phase heat flow and cumulative heat release, as measured by isothermal calorimetry. The silicate peak can be clearly distinguished in all of the specimens, with the acceleration of cement hydration in the presence of NS evident in both an increment in the exothermic peak value, as well as in the decreased silicate peak occurrence time (Fig. 7a). It can be seen that increments in the NS dosage resulted in gradual decrements in the time of occurrence of the silicate peak. The maximum heat flow value of the silicate peak was found

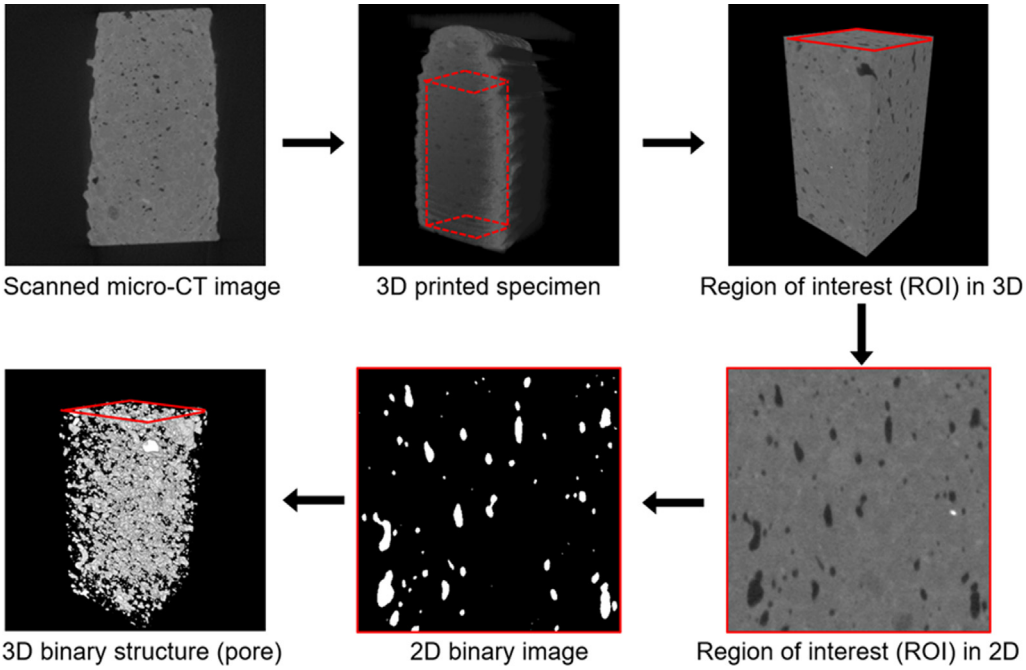

Fig. 6. Micro-CT imaging procedure for classifying pore structure (3NS) (Note: in the 2D and 3D binary images, the white represents pores within the specimen.)

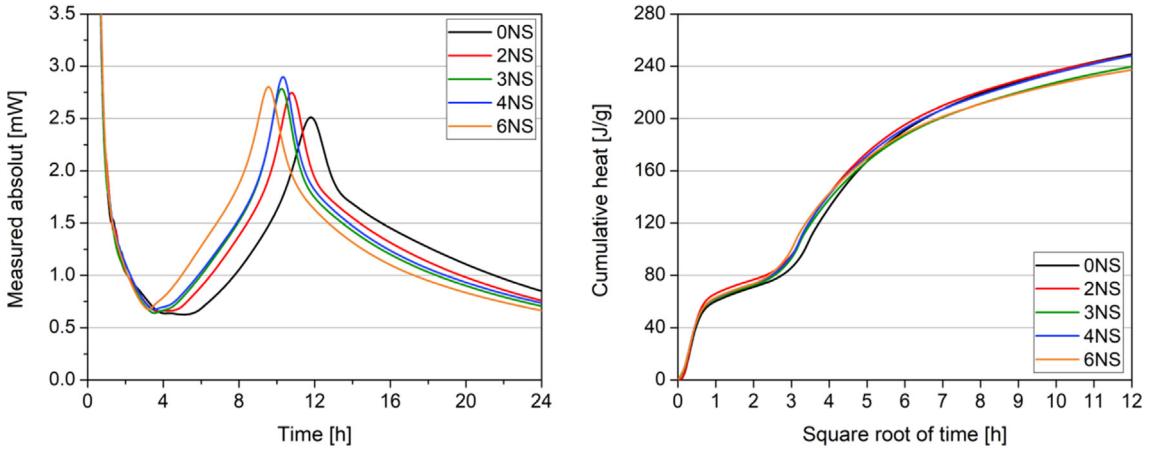

Fig. 7. Heat flow (left) and cumulative heat (right) of printable mortars.

to have occurred for specimen 4NS, being 15% higher than that of specimen 0NS. In addition, the time required to reach the maximum exothermic peak decreased from 11 h 48 min (0NS) to 10 h 20 min. The exothermic peak occurred fastest in specimen 6NS, after 9 h and 34 min. The beneficial effect of NS on the acceleration of the binder hydration process can be attributed to the ultrafine size of NS particles, which act as a nucleus for cement hydration, thus leading to faster formation of calcium hydroxide (CH) and more dynamic consumption of the tricalcium silicate (C_3S) phase during the binding period [56–58]. However, no significant effect of NS on the cumulative heat (Fig. 7b) was observed at up to 144 h of hydration, with only a marginal difference of 4% occurring between specimens.

4.2. In-situ XRD

Fig. 8 represents the normalized reflex intensity development of the 024 C_3S reflex and the 001 portlandite reflex, over the first 24 h of hydration, as measured by in-situ XRD. Fig. 8a shows that the decrease of the 024 C_3S reflex occurred latest for the sample without any NS. Accordingly, in Fig. 8b, this sample showed the latest increase in portlandite reflex intensity. The results presented in Fig. 8b further show the clear trend of increasing amounts of NS reducing the time until portlandite can be detected by XRD. These results further support the trend of increasing amounts of NS causing more dynamic C_3S consumption, accompanied by faster CH formation, as was observed through isothermal calorimetry.

Although for purpose of calorimetry and in-situ XRD study of the binder hydration process the SP dosage needed to be increased, the study provided valuable knowledge on the hydration process of printable binder. As shown in previous study of Tobon et al. [59], the dynamics of hydration process is noticeably different in NS-cement-limestone than in pure cement-NS systems. Therefore, it was of high importance to evaluate to what extent NS can affect the hydration process of high-volume limestone binder proposed in our study for 3D printing.

4.3. Rheological measurements

Fig. 9 represents the evolution of shear-stress, as a function of the shear-rate for all the printable mortars used in this study. Two observations can be made: (i) All the mortars showed a yield-stress, which is a finite value of the shear-stress at low shear-rate value, according to the presence of a stress plateau at low shear-rate values. This value is increasing with NS concentration. Moreover, at high NS concentration, a strong thixotropic [60] behavior is observed as shear-stress decreases with the shear-rate at very low shear-rate. (ii) No significant differences were found at high shear-rates, indicating that the plastic viscosities of these mortars were similar to one another. The correlation between yield-stress and NS concentration has already been reported, with the effect attributed to the extremely high surface area of NS, which thus leads to nanoparticles' higher water demand, consequently resulting in a reduction of fluidity [56]. Differences

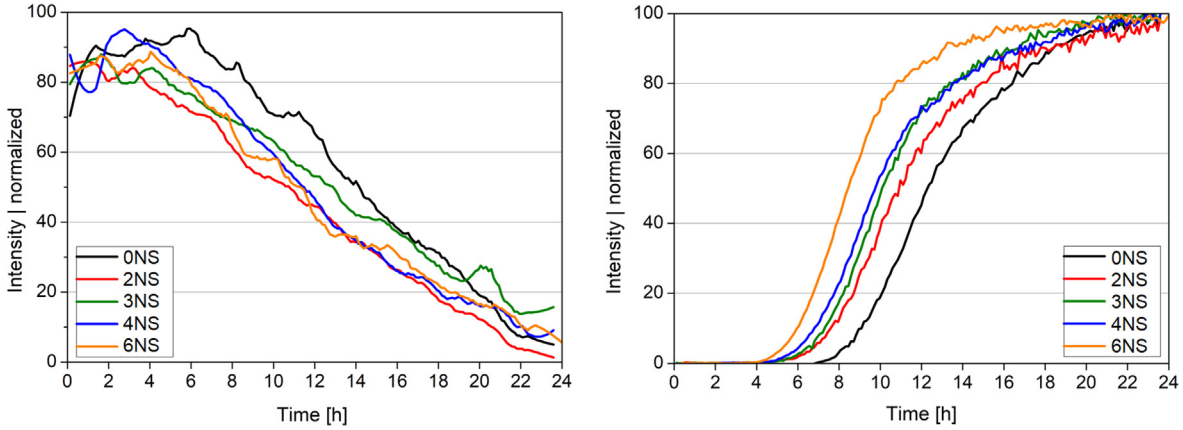

Fig. 8. Normalized reflex intensity development measured by in-situ XRD of 024 C_3S reflex (left) and 001 portlandite reflex (right). (Note: C_3S reflex curve was smoothed to increase readability of the results).

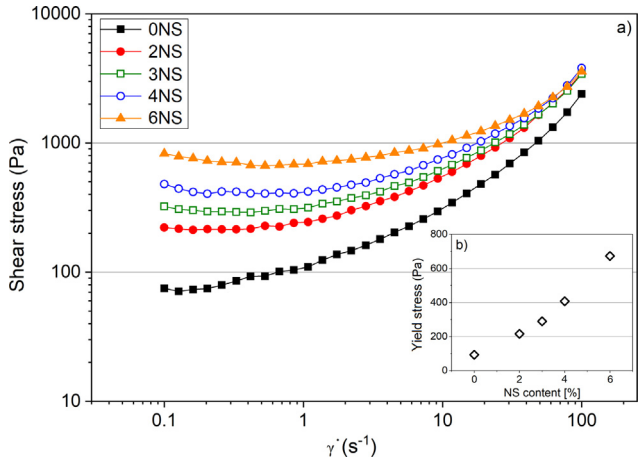

Fig. 9. Shear-stress as a function of the shear-rate of printable mortars with different NS contents (a) and yield-stress at 0.4 s^{-1} vs. NS dosage (b).

in viscosity decrease with the shear-rate, proving that NS changes the microstructure of the mortar at rest, due to stronger flocculation of the particles in the system, rather than because of an increase in the solid content. The increase of the yield-stress can only be explained by the increase of the NS concentration, as the slight increase of SP would rather lead to a decrease of the yield stress with its concentration.

As can be seen in Fig. 9b, the yield-stress for the range of NS concentrations tested seemed to increase linearly with NS concentration; the equation associated with this linear increase is $\tau_y(Pa) = 96.5 \cdot NS(\%) + 46$. This effect has previously been observed [8], for a different mix design, with linear parameters in the same order of magnitude.

The tests outlined above show that NS can be efficiently used to increase the yield-stress of a mortar and thus its capacity to withstand more layers stacked on top of each other. As a result, it is possible to print more layers at the same time and therefore speed up the printing process. However, it is also evident that shear-stress, in the typical shear-rate pumping range (5–20 s^{-1}), also increases with the addition of NS, thus requiring a higher pressure to pump out the mortar, as pressure is proportional to mortar viscosity.

4.4. Setting time and strength evolution of printable mortar

Fig. 10a represents the initial and final mortar setting times values, while Fig. 10b depicts mortars' strength evolution during the first 10 h of hydration. It can be seen that strength developed rapidly after the occurrence of specimens' final setting. Increasing the dosage of NS resulted in a decrement in initial and final setting times. Moreover, a shortening of the interval between the initial and final set was observed. Similar findings have been reported by other researchers [61,62]. All NS-modified specimens exhibited significantly increased strength, as compared to the 0NS specimen, at up to 6 h of hydration. The differences between the results were smaller after this period.

4.5. Penetration test

The evolution of mortar strength as a function of time, as calculated from the force data, is shown in Fig. 11, for all the printable mortars tested. All the curves display a similar trend, with strength evolving slowly in the beginning, a few minutes after mixing, followed by faster strength increase with time, as characterized by the slope. The point at which acceleration occurred depended strongly on the NS concentration: the higher the NS content, the faster the strength gain. Moreover, the strength evolution slope also increased with NS dosage. These results support the ultrasound data, with the value obtained for the initial setting time (0.1 MPa) showing a similar trend. In addition, the penetration measurement shows that, while yield-stress increases with the addition of NS, mortar open time decreases with NS addition; in some cases, the mix formulation used might have to be adapted so as to have a longer open time, by the addition of retarders, for example. Due to the exothermic behavior of the cementitious mortars, the penetrometer tests showed faster kinetics when compared to ultrasonic tests or calorimetry, because their sample volume was much higher than size of specimens for ultrasonic or calorimetry tests, leading to auto-acceleration as the result of temperature increase.

Observed phenomena related to the substantial alteration of the fresh properties of printable mortar in presence of NS is attributed to high activity of NS within the binder phase of printable mortars, which was confirmed by our calorimetric and in-situ XRD study. Due to seeding effect of silica nanoparticles [63,64] earlier formation of C-S-H phase occurs, and in turn substantial effect on the thixotropic properties and early strength development of mortars.

4.6. Oven-dry density and thermal conductivity

Table 2 presents the results of the oven-dry density and thermal conductivity tests of the printable mortars. The incorporation of NS did not affect their density, but a slight drop in thermal

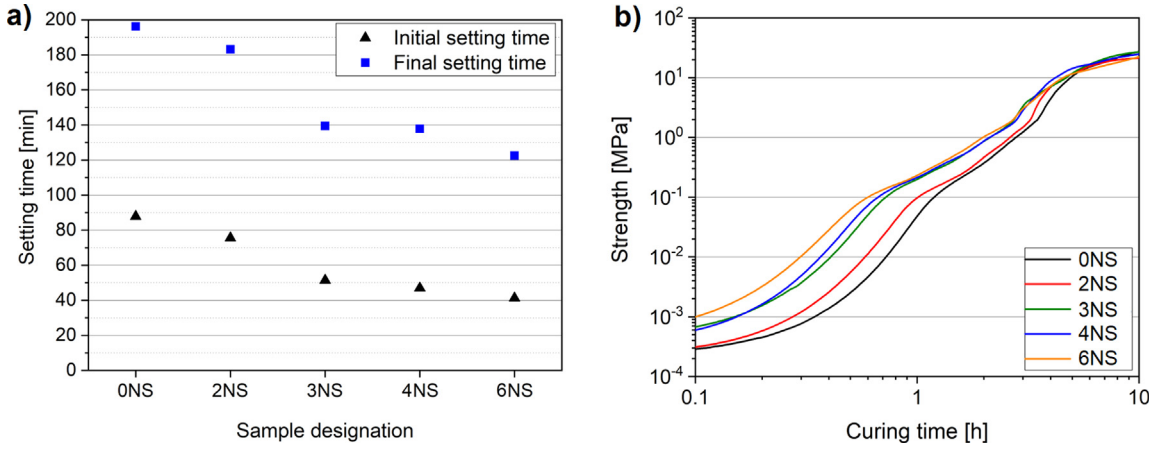

Fig. 10. Setting times (a) and strength development (b) of printable mortars, obtained with an ultrasonic device.

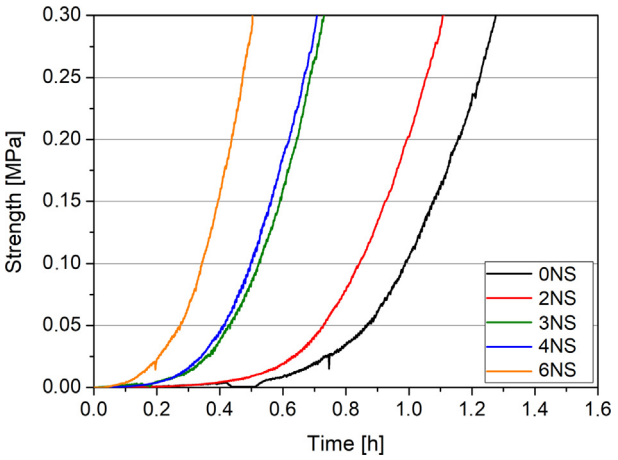

Fig. 11. Strength development determined from penetration measurements.

conductivity resulted from increases in NS dosages. While it has been reported that higher concentrations of NS might contribute to slight decreases in the thermal conductivity of cementitious composites [65,66], in the present work the differences were marginal.

4.7. Compressive strength

The compressive strength of the casted and printed mortars after 7 and 28 days is depicted in Fig. 12. In general, printed specimens exhibited lower compressive strength values than casted specimens from 8% to 14%, with the highest discrepancy for 6NS followed by 4NS. However, in both printed and casted specimens, similar trends of compressive strength can be observed. After 7 d of curing, casted specimens exhibited compressive strength values above 60 MPa and that in all cases, specimens exhibited over 80% of their 28 d strength. In case of printed samples, specimens 0NS and 6NS exhibited strength values below 60 MPa after 7 d of curing.

The highest compressive strength of casted and printed mortars, after 7 d of curing, was obtained by specimens 2NS and 3NS. Casted mortars exhibited compressive strengths 12% (2NS) and 11% (3NS) higher than that of 0NS, while 2NS and 3NS printed specimens exhibited 13% higher strengths than 0NS. After 28 d of curing, casted specimens 2NS and 3NS exhibited 17% and 10% higher compressive strengths, as compared to 0NS. In case of printed specimens 2NS and 3NS exhibited 18% and 8% higher compressive strengths when compared to 0NS. A higher dosage of NS resulted in gradual decrement of the beneficial effects of NS on the mechanical performance of specimens, with the 6NS specimen exhibiting already comparable strength to that of the reference specimen. Therefore, our study found that there is an optimal amount of NS which is beneficial for improving the compressive strength of printed mortars. In addition, after 28 d the strength improvement was even more noticeable in 2NS specimen. The beneficial effect of NS on the compressive strength of specimens is mainly attributable to three synergistic effects: the nucleation effect, the nano-filling effect and pozzolanic activity. Accordingly, the presence of NS in a mixture results in a more refined and compact microstructure; the reaction of NS particles with calcium hydroxide (CH) leads to an increase in the amount of calcium silicate hydrate (C-S-H) gel in the reaction. Moreover, the ultrafine NS particles fill the voids in the cement matrix, which results in decreased paste porosity and an optimized distribution of the pore structure [31]. Due to the low w/b ratio and significant contribution of fines even limited dosage of NS in the mortar system resulted in noticeable strength improvement. Nevertheless, when the amount of NS exceeded the optimal value specimens with higher NS contents the decreasing trend of strength was observed. This effect is attributed to excessive binder hydration reaction process in the early hours of hydration as well as possible agglomeration of the NS which results in creation of so-called "weak zones" [67] in the cementitious matrix resulting in deterioration of the mechanical performance of specimens. In addition, slightly higher discrepancies between compressive strength values of printed and casted 4NS and 6NS specimens were observed. This can be attributed to higher volume of larger pores in these specimens as a result increased thixotropy of specimens, reported in Section 4.3, and thus possible difficulties in extrusions. This phenomenon will be described in further part of the manuscript (Sections 4.10 and 4.11).

Table 2
Oven-dry density and thermal conductivity of printable mortars.

Sample designation	Oven-dry density [g/cm^3]	Thermal conductivity [W/m·K]
0NS	1.941	1.38
2NS	1.940	1.39
3NS	1.935	1.30
4NS	1.942	1.34
6NS	1.946	1.32

4.8. Transport properties

The results of water accessible porosity and water absorption coefficients are presented in Fig. 13. Incorporation of NS in printable mortars resulted in the production of a denser mortar matrix and thus the water accessible porosity and water absorption coefficients were low. In general, a gradual improvement in transport properties with increments in NS dosage was observed. NS-modified specimens exhibited a decrease of 5% to 12% of water accessible porosity and a decrease of 25% to 39% of the water absorption coefficient. The present study therefore confirms that NS has a beneficial effect in improving the transport properties of printable mortars. To provide deeper insight into this phenomenon, MIP evaluation was also performed, as outlined below.

4.9. Mercury intrusion porosimetry

Table 3 presents selected properties of printable mortars obtained with MIP analysis. Incorporation of NS, in an optimal dosage ranging between 2 and 3 wt-%, decreased the total (Hg) intruded volume, thus confirming that specimens with NS exhibited lower porosity than 0NS. Furthermore, decreased average and median pore diameters were reported for NS dosages of up to 3 wt-%. With higher NS dosages, the intrusion volume increased slightly. Moreover, slightly higher average pore diameter and median pore diameter (excluding 6NS) was observed, which does not correlate directly with the results of transport properties. However, to understand this phenomenon, the evaluation of the pore size distribution is required.

It is generally agreed that pore volume size have a noticeable effect on the transport and mechanical properties of cementitious composites [68–70], with different pore size classifications available in the literature [71,72]. According to Wu and Lian [70], pores in concrete can be divided into four types: d < 0.02 μm (harmless pore), d = 0.02–0.05 μm (less harmful pore), d = 0.05–0.20 μm (harmful pore), d > 0.20 μm (more harmful pore). In addition, it has been suggested that increasing the number of pores with d < 0.05 μm while reducing the number of those with d > 0.1 μm, can improve concrete performance. Alternatively, Mehta and Monteiro [68] have proposed a different concrete pore distribution

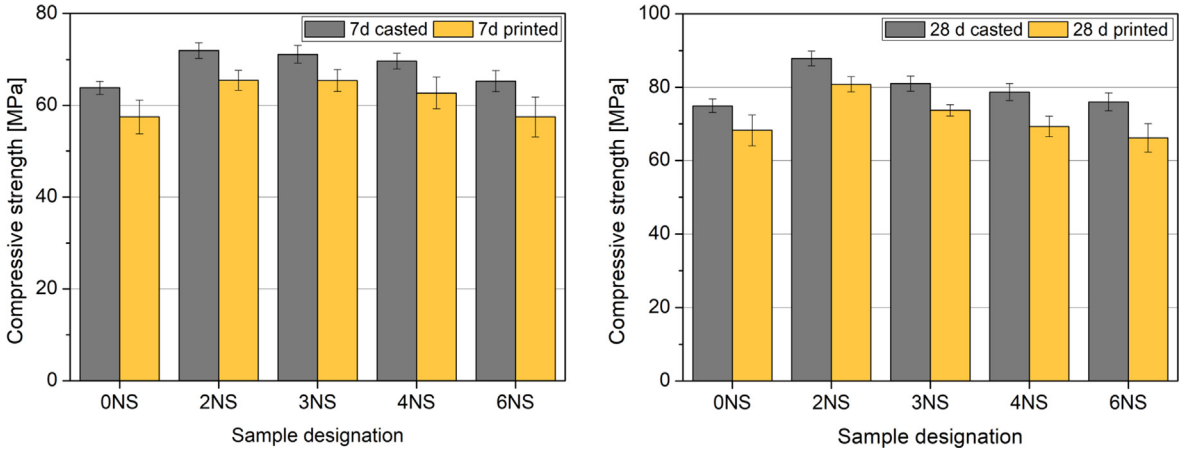

Fig. 12. Compressive strength of casted and printed specimens after 7 (left) and 28 days (right) of curing.

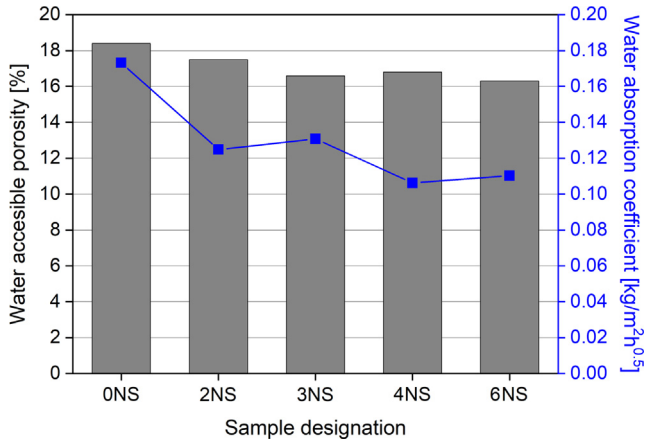

Fig. 13. Water accessible porosity and water absorption coefficient of printable mortars.

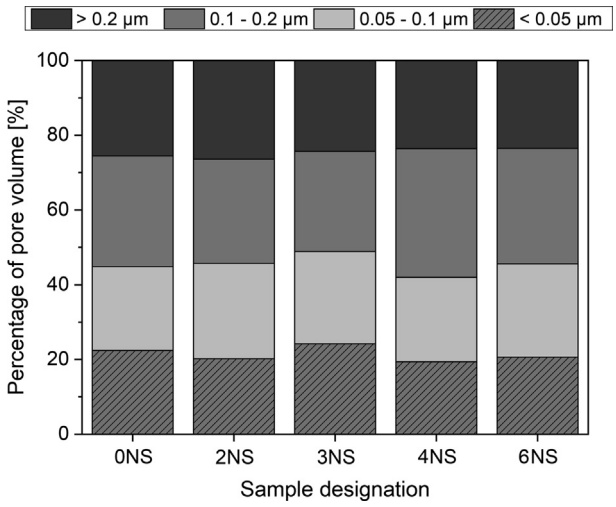

Fig. 14. Percentage of pore distribution of printable mortars obtained by MIP.

range: d > 0.10 μm (more harmful pore), d = 0.05–0.10 μm (harmful pore), d = 0.0045–0.05 μm (less harmful pore), d < 0.0045 μm (harmless pore); with the suggestion that when d < 0.05 μm, the pores will exert less impact on strength and permeability. However, the present study shows that, besides a decrement in the total porosity of specimens 2NS and 3NS (Table 3), there was a noticeable increment of pores in the range < 100 nm, along with a decrement of harmful pores volume (Fig. 14). According to the literature [31,73,74], NS particles act as nucleation sites in pore solutions, resulting in a uniform distribution of hydration products within the cement matrix. Moreover, the presence of NS in the mixture also results in the formation of an additional amount of C-S-H phase, as well as in an improvement in the interfacial transition zone (ITZ) between the cement matrix and the aggregate. Besides its chemical activity, NS also acts as a nano-filler, filling the pores between hydration products. These synergistic effects result in a significant densification of the microstructure, as well as a refinement of the pore structure of cementitious composites. Although the specimens with higher NS dosages – 4NS and 6NS – actually exhibited slightly increased total porosity, as compared to the 0NS specimens (Table 3), their transport properties were still improved. This confirms the findings of other researchers [75–77] that, despite the total porosity of NS-modified specimens possibly remaining comparable to that of non-modified specimens, the significant alteration of pore structure through the disconnection of continuous pores from discontinuous ones and the subdivision of larger pores into smaller ones, changes the shape of pores as well as their tortuosity. Therefore, despite some properties (such as compressive strength) deteriorating as a result of excessive NS content, certain characteristics, such as water sorptivity, continued to improve, as a result of pore structure alteration.

4.10. Micro-computed tomography

The characteristics of the printed specimens were also examined using the micro-CT images obtained. For all specimens with

Table 3
The results of MIP analysis of printable mortars.

	0NS	2NS	3NS	4NS	6NS
Total intruded vol. [mm³/g]	83.46	82.63	80.68	86.37	86.91
Average pore diameter [μm]	0.0556	0.0588	0.0527	0.0598	0.0591
Median pore diameter [μm]	0.1218	0.1199	0.1120	0.1282	0.1193

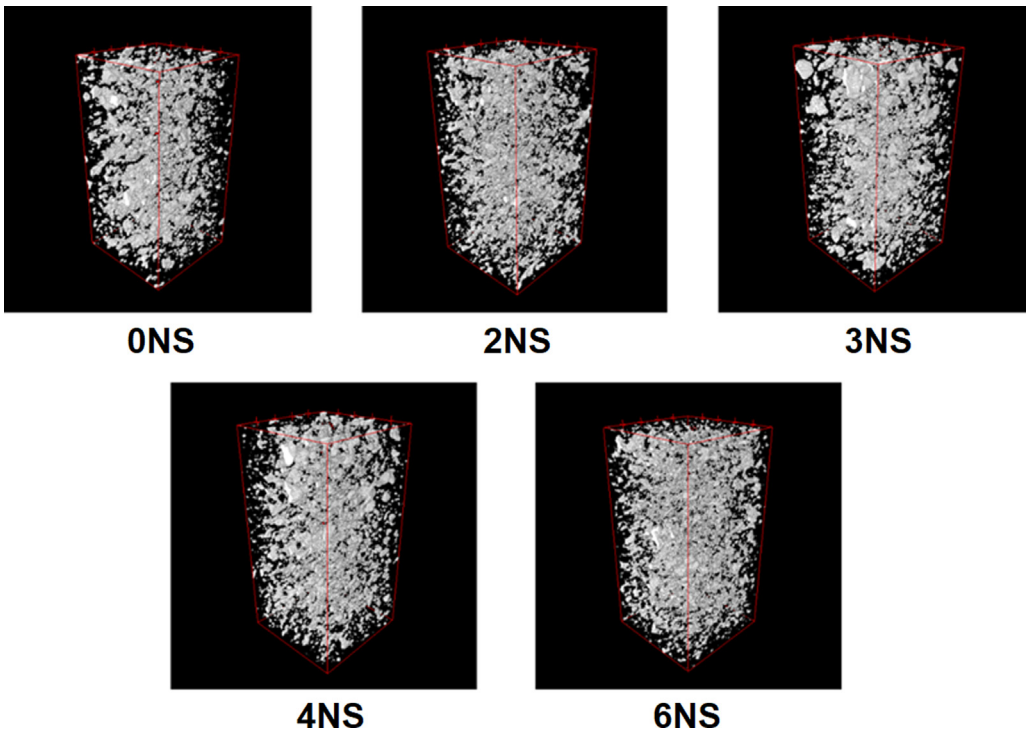

Fig. 15. Pore structures of the specimens obtained from micro-CT images (Note: the white represents pores within each specimen).

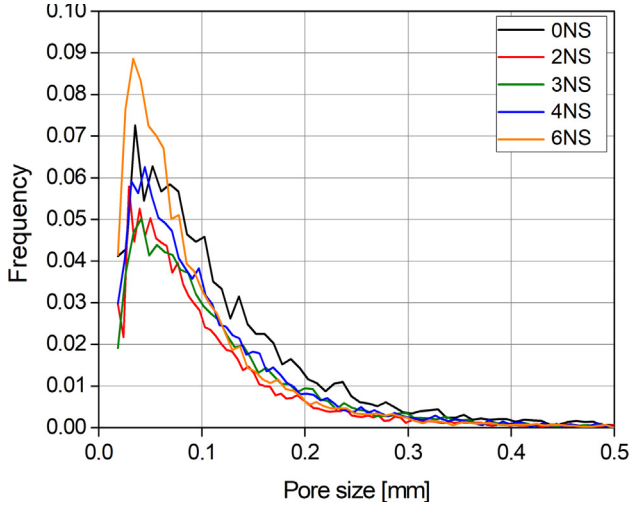

Fig. 16. Void size distribution in 3D printed specimens obtained from micro-CT.

or without nanosilica, the same volume of the ROIs was selected and compared. Fig. 15 shows the pore structures within the specimens obtained using micro-CT images. The volumes of voids in these specimens was calculated as being 4.82, 4.25, 4.59, 4.31 and 4.30% for 0NS, 2NS, 3NS, 4NS and 6NS, and these values only considered the pores larger than the image resolution (30 μm) Fig. 16 represents the specimen pore size distributions computed from the pore images in Fig. 15; the proportion of pores > 0.1 mm was lower in the 2NS and 3NS specimens, than in the other cases. The highest proportion of larger pores can be seen in the specimen 6NS. In general, it was confirmed that relatively large pores contribute to a reduction in the mechanical properties of materials [78,79] and this pore size distribution trend is in line with the compressive strength results of this study as well as the higher discrepancy between results of casted and printed specimens.

Moreover, as can be seen from Fig. 15, the features of the pore structure in each specimen seem to have be similar. Unlike general pores, which are almost spherical, the pores in the printed specimens were anisotropic; denoting that the pores inside the printed samples had a directional dependency. As demonstrated in previous studies [80,81], these anisotropic pores strongly affect material characteristics and properties, with a detailed investigation of the pores needed to better understand the printed materials. Figs. 17 and 18 show the results of the probability functions of specimens 0NS and 2NS, which were chosen as being representative. Extended versions of Figs. 17 and 18, covering all the specimens measured in this study, are available in the Supplementary Materials (Figs. S1 and S2). As can be seen from the images, all cases presented relative pore clustering in different x, y and z directions. In the functions of each specimen, the pore size in the x-direction was the largest, while the y-direction showed the smallest length among the three directions. This indicates that the pores inside the printed specimens tended to be elongated in the x-direction, while being compressed in the y- and z-directions.

For the quantitative anisotropy comparison, parameters computed by integrating the P_2 and L_2 functions were utilized. As can be seen in Figs. 17 and 18, the probability functions are the form of 2D graphs, which are difficult to index. To overcome this limitation, an integrated parameter has been proposed and confirmed as effectively representative [82]; the detailed procedure is presented therein [82], with the results obtained presented in Table 4. The table contains the integrated parameters computed from the results in Figs. 17 and 18 and the maximum differences that can index anisotropy. The degree of anisotropy of pore clustering and pore size can be evaluated from the maximum differences of both P2 and L2. Among the parameters calculated, the maximum differences of 2NS in P2 and L2 were the smallest, meaning that the 2NS specimen contained less anisotropic pores and therefore, that the 2NS specimen was least affected by the printing procedure, as well as that the amount of nanosilica in the 2NS specimen effectively reduced pore anisotropy during the printing process.

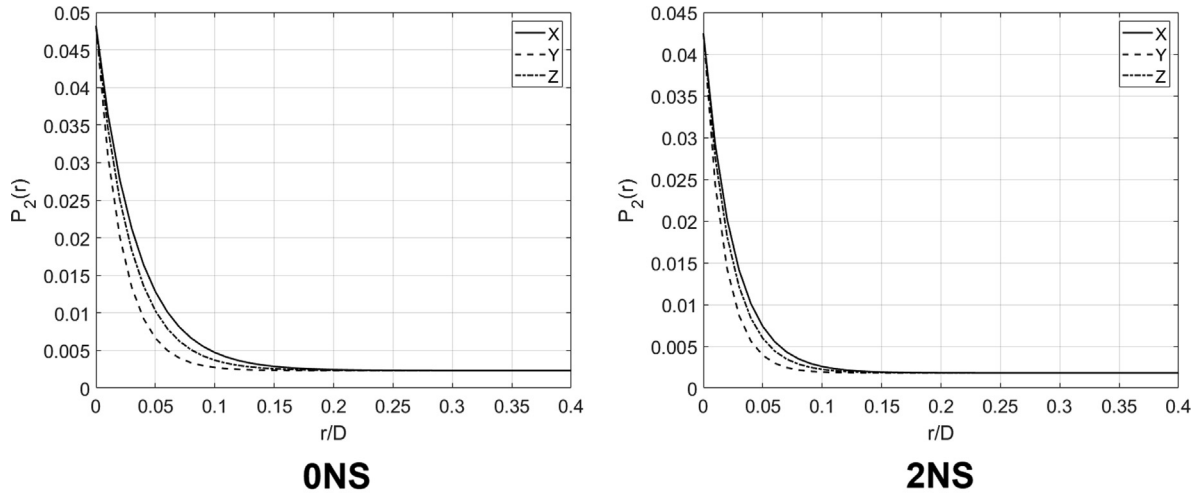

Fig. 17. Two-point correlation function (P2) of 0NS and 2NS in x, y and z directions (Note: D is the specimen length, while r is the distance between two random points.)

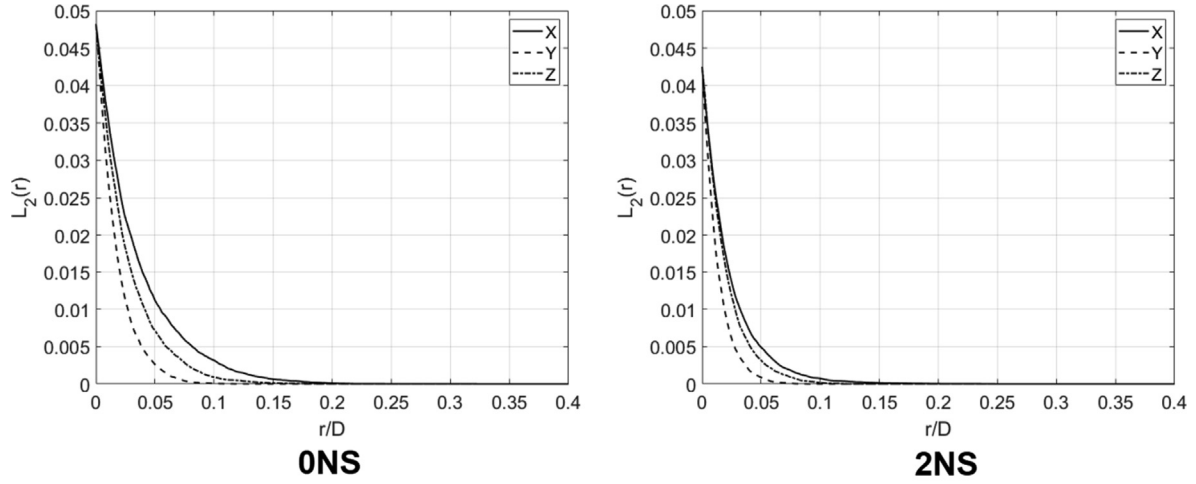

Fig. 18. Lineal-path function (L_2) of 0NS and 2NS in x, y and z directions (Note: D is the specimen length, while r is the length of a test line).

Table 4
Integrated parameters for anisotropy measurements.

	P2				L2			
	x-dir.	y-dir.	z-dir.	Max. difference	x-dir.	y-dir.	z-dir.	Max. difference
0NS	0.0039	0.0033	0.0036	0.0833	0.0017	0.0008	0.0013	0.3077
2NS	0.0028	0.0025	0.0027	0.0370	0.0009	0.0005	0.0008	0.1703
3NS	0.0035	0.0030	0.0033	0.0606	0.0015	0.0007	0.0012	0.2500
4NS	0.0030	0.0026	0.0028	0.0714	0.0011	0.0006	0.0009	0.2222
6NS	0.0028	0.0025	0.0027	0.0370	0.0009	0.0005	0.0007	0.1836

The solid characteristics of the printed samples were also evaluated using micro-CT images. As discussed earlier, the grey-scale value of the micro-CT images indicates the relative density of the target object, with a comparison of the pixel values and the distribution of the pixel value along the z-direction (height) shown in Fig. 19. Despite the fluctuation that can be observed, the maximum difference among the values was about 8 in grey-scale value. This difference can be used to confirm that the specimens were generally as homogenous as conventional concrete [14]. In addition, there was no significant fluctuation in any single printed layer, thus demonstrating that the printing procedure did not affect the homogeneity of the material. Regarding the mean solid values of the whole specimen, 2NS had the highest value among the NS specimens, although the difference and relative density decreased with increasing nanosilica content.

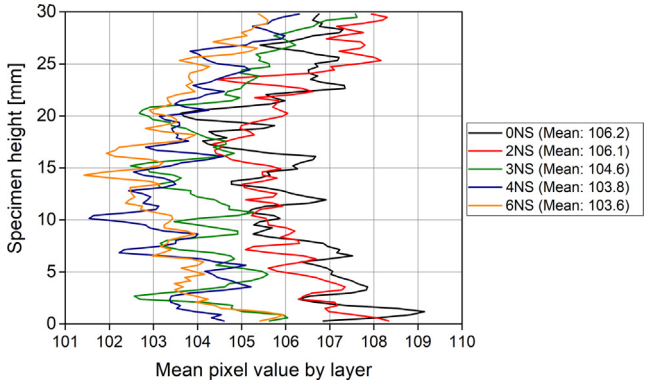

Fig. 19. Mean pixel value vs. specimen height and mean pixel value.

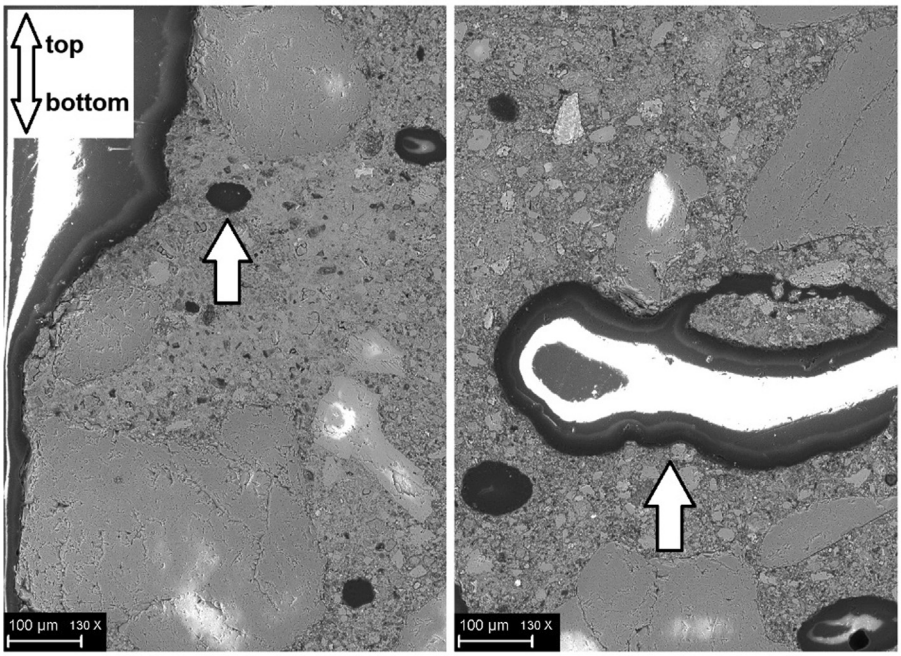

Fig. 20. SEM micrographs of specimen 0NS: connection between layers (left) and inner part of the specimen (right). Note: Arrows indicate examples of anisotropic pores.

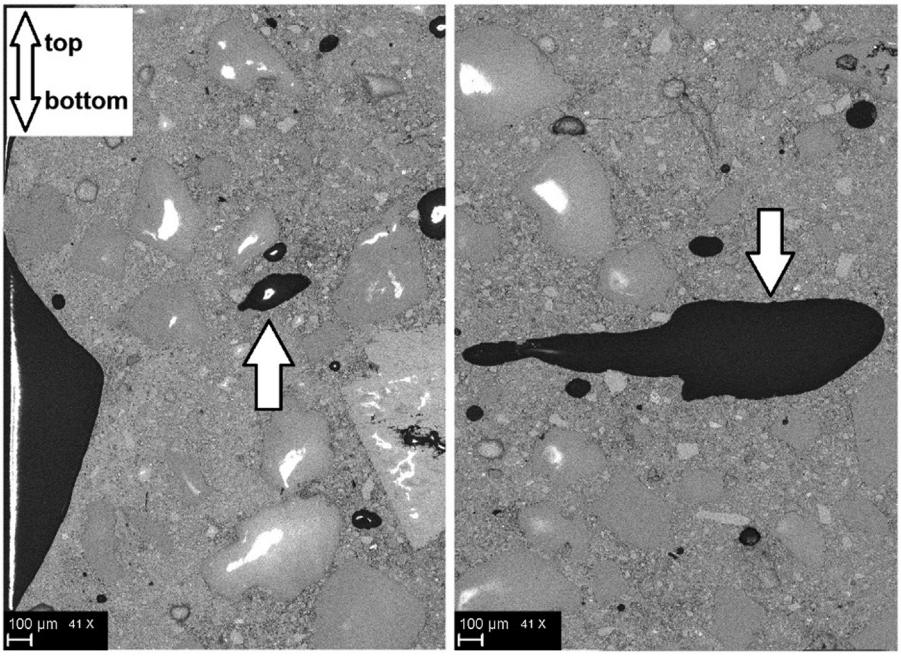

Fig. 21. SEM micrographs of specimen 3NS: connection between layers (a) and inner part of specimen (b). Note: Arrows indicate examples of anisotropic pores.

The effects of NS on the microstructures of the printed material can be confirmed by the results obtained from the micro-CT investigation. Appropriate usage of NS can reduce the proportion of large pores which can affect material strength, while reducing pore anisotropy. In addition, the reduction of solid density can be adjusted by controlling NS content.

4.11. Scanning electron microscopy

SEM micrographs of the selected specimens are presented in Figs. 20–22. 0NS, 3NS and 6NS were chosen as representative and tested. No noticeable differences were observed in porosity between the bulk and interlayer parts, or between the inner

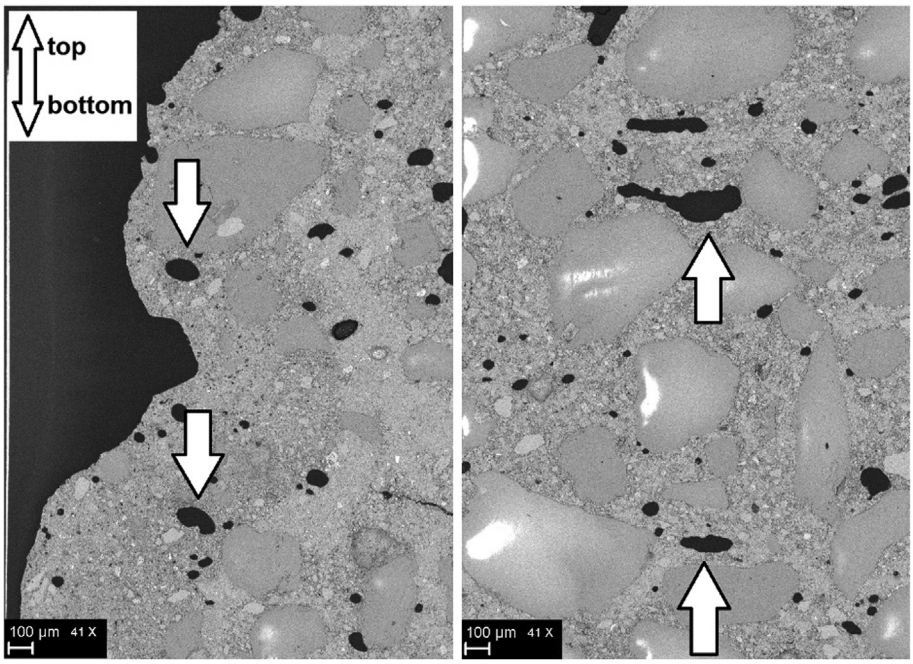

Fig. 22. SEM micrographs of specimen 6NS: connection between layers (a) and inner part of specimen (b). Note: Arrows indicate examples of anisotropic pores.

and outer parts of the 3D printed mortar. Unreacted cement clinker and a significant fraction of limestone filler, which is known to be nearly inert, can be distinguished in all specimens. Besides the nearly spherical pores, elongated pores in the x-direction can be discerned, confirming findings regarding pore anisotropy in 3D printed elements [12,14,30]. However, in the present study, pores were located evenly in the bulk and inter-layer region. Also, a higher amount of large pores, with sizes ranging from 0.1 to 0.2 mm, were measured in specimen 6NS (Fig. 20), as compared to specimens 0NS and 3NS, which is line with the results of micro-CT evaluations (Fig. 16). It can therefore be concluded, on the basis of both the micro-CT and SEM evaluations, that the incorporation of NS has a beneficial effect on the buildability of printable mortars, as the anisotropy of pores is thus decreased. However, if the amount of NS exceeds the optimum required dosage, the thixotropy of the printable mixture increases significantly, leading to possible difficulties in extrusion, which might, in turn, result in an increase in the amount of voids produced in the specimen. A similar observation has been reported in other research [13], where clay nanoparticles contributed to an increase in interlayer-bonding porosity, despite their beneficial effects on 3D printed concrete performance.

5. Conclusions

This study has investigated the effects of various dosages of nanosilica on the fresh and hardened properties of 3D printable mortars. The following conclusions can be drawn:

1) Nanosilica has a significant effect on the acceleration of hydration of the binder phase in printable mortars. Incorporation of NS to the mix results in the faster formation of calcium hydroxide (CH) and more dynamic consumption of tricalcium silicate (C_3S) phase. Ultrasound and penetration measurements confirmed that the setting and hardening process of mortar is accelerated when NS is present in the mixture. Open time is shortened with an increase in NS dosage.
2) The incorporation of NS noticeably affects rheology by increasing mortar yield-stress, thus increasing its capacity to bear additional layers. Nevertheless, the shear-stress value also increases with the addition of NS, thus increasing the pressure required to pump out NS-modified mortar.
3) A significant improvement in 7 d and 28 d compressive strength was reported, when an optimal amount of NS was incorporated into the mixture. Beyond this amount, compressive strength decreased and was comparable to that of the control specimen.
4) Substantial improvements in the transport properties of printable mortars was observed, even when the NS dosage exceeded the optimal value. MIP analysis confirmed that NS contributes to the refinement of the pore structure, thus improving the impermeability of mortars.
5) Micro-CT and SEM studies confirmed anisotropy in the pore characteristics of 3D printed elements. Incorporation of NS is beneficial in improving the buildability of printable mortars, thus, decreasing pore anisotropy.

Overall, this study firstly has utilized the microstructural characteristics of 3D printable mortars incorporating NS using several techniques including micro-CT. The obtained results have shown that, despite different mixture composition when compared to conventional cement mortars and concretes, NS has a substantial effect on fresh and hardened properties of 3D printable type of mortars. The proposed evaluating method based on micro-CT can be further utilized for the characteristics of construction materials to optimize their buildability.

Funding

This project received funding from the European Union's Horizon 2020 research and innovation program, as part of Marie Skłodowska-Curie Grant agreement no. 841592.

CRediT authorship contribution statement

Pawel Sikora: Conceptualization, Methodology, Validation, Formal analysis, Data curation, Investigation, Writing - original draft, Writing - review & editing, Project administration, Funding acquisition. **Sang-Yeop Chung:** Methodology, Software, Formal analysis, Data curation, Writing - review & editing, Visualization. **Maxime Liard:** Investigation, Formal analysis, Visualization, Writing - original draft. **Didier Lootens:** Methodology, Software, Resources, Writing - review & editing, Supervision. **Tobias Dorn:** Investigation. **Paul H. Kamm:** Investigation, Resources. **Dietmar Stephan:** Resources, Supervision, Project administration, Writing - review & editing. **Mohamed Abd Elrahman:** Investigation.

Declaration of Competing Interest

The authors declare that they have no known competing financial interests or personal relationships that could have appeared to influence the work reported in this paper.

Acknowledgement

We would like to thank Christian Lehmann from TU Berlin and Philipp Drabetzki from Federal Institute for Materials Research and Testing (BAM) for supporting this research with SEM and MIP measurements, respectively.

Appendix A. Supplementary data

Supplementary data to this article can be found online at https://doi.org/10.1016/j.conbuildmat.2021.122574.

References

[1] J. Prinsloo, S. Sinha, B. von Solms, A review of industry 4.0 manufacturing process security risks, Appl. Sci. 9 (2019) 5105, https://doi.org/10.3390/app9235105.
[2] M. Kaszyńska, S. Skibicki, M. Hoffmann, 3D concrete printing for sustainable construction, Energies 13 (23) (2020), https://doi.org/10.3390/en13236351.
[3] B. García de Soto, I. Agustí-Juan, J. Hunhevicz, S. Joss, K. Graser, G. Habert, B.T. Adey, Productivity of digital fabrication in construction: cost and time analysis of a robotically built wall, Autom. Constr. 92 (2018) 297–311, https://doi.org/10.1016/j.autcon.2018.04.004.
[4] M. Valente, A. Sibai, M. Sambucci, Extrusion-based additive manufacturing of concrete products: revolutionizing and remodeling the construction industry, J. Compos. Sci. 3 (2019) 88, https://doi.org/10.3390/jcs3030088.
[5] S.C. Paul, Y.W.D. Tay, B. Panda, M.J. Tan, Fresh and hardened properties of 3D printable cementitious materials for building and construction, Arch. Civil Mech. Eng. 18 (2018) 311–319, https://doi.org/10.1016/j.acme.2017.02.008.
[6] R.A. Buswell, W.R. Leal de Silva, S.Z. Jones, J. Dirrenberger, 3D printing using concrete extrusion: A roadmap for research, Cem. Concr. Res. 112 (2018) 37–49, https://doi.org/10.1016/j.cemconres.2018.05.006.
[7] G. Ma, L. Wang, Y. Ju, State-of-the-art of 3D printing technology of cementitious material—An emerging technique for construction, Sci. China Technol. Sci. 61 (2018) 475–495, https://doi.org/10.1007/s11431-016-9077-7.
[8] O.A. Mendoza Reales, P. Duda, E.C.C.M. Silva, M.D.M. Paiva, R.D.T. Filho, Nanosilica particles as structural buildup agents for 3D printing with Portland cement pastes, Constr. Build. Mater. 219 (2019) 91–100, https://doi.org/10.1016/j.conbuildmat.2019.05.174.
[9] G. de Schutter, K. Lesage, V. Mechtcherine, V.N. Nerella, G. Habert, I. Agusti-Juan, Vision of 3D printing with concrete — technical, economic and environmental potentials, Cem. Concr. Res. 112 (2018) 25–36, https://doi.org/10.1016/j.cemconres.2018.06.001.
[10] A.V. Rahul, M. Santhanam, H. Meena, Z. Ghani, Mechanical characterization of 3D printable concrete, Constr. Build. Mater. 227 (2019), https://doi.org/10.1016/j.conbuildmat.2019.116710 116710.
[11] M. Moini, J. Olek, J.P. Youngblood, B. Magee, P.D. Zavattieri, Additive manufacturing and performance of architectured cement-based materials, Adv. Mater. Weinheim. 30 (2018), https://doi.org/10.1002/adma.201802123 e1802123.
[12] J. van der Putten, M. Deprez, V. Cnudde, G. de Schutter, K. van Tittelboom, Microstructural characterization of 3D printed cementitious materials, Materials (Basel) 12 (2019), https://doi.org/10.3390/ma12182993.
[13] B. Panda, N.A. Noor Mohamed, S.C. Paul, G. Bhagath Singh, M.J. Tan, B. Šavija, The effect of material fresh properties and process parameters on buildability and interlayer adhesion of 3D printed concrete, Materials (Basel) 12 (2019), https://doi.org/10.3390/ma12132149.
[14] H. Lee, J.-H.-J. Kim, J.-H. Moon, W.-W. Kim, E.-A. Seo, Correlation between pore characteristics and tensile bond strength of additive manufactured mortar using X-ray computed tomography, Constr. Build. Mater. 226 (2019) 712–720, https://doi.org/10.1016/j.conbuildmat.2019.07.161.
[15] E. Keita, H. Bessaies-Bey, W. Zuo, P. Belin, N. Roussel, Weak bond strength between successive layers in extrusion-based additive manufacturing: measurement and physical origin, Cem. Concr. Res. 123 (2019), https://doi.org/10.1016/j.cemconres.2019.105787 105787.
[16] D.P. Bentz, S.Z. Jones, I.R. Bentz, M.A. Peltz, Towards the formulation of robust and sustainable cementitious binders for 3-D additive construction by extrusion, Constr. Build. Mater. 175 (2018) 215–224, https://doi.org/10.1016/j.conbuildmat.2018.04.167.
[17] T. Dorn, T. Hirsch, D. Stephan, Study on the influence of accelerators on the hydration of portland cement and their applicability in 3D printing, in: V. Mechtcherine, K. Khayat, E. Secrieru (Eds.), Rheology and Processing of Construction Materials, Springer International Publishing, Cham, 2020, pp. 382–390.
[18] T. Hirsch, T. Dorn, D. Stephan, Early properties of portland cements with varied set regulators, in: V. Mechtcherine, K. Khayat, E. Secrieru (Eds.), Rheology and Processing of Construction Materials, Springer International Publishing, Cham, 2020, pp. 97–105.
[19] D. Marchon, S. Kawashima, H. Bessaies-Bey, S. Mantellato, S. Ng, Hydration and rheology control of concrete for digital fabrication: potential admixtures and cement chemistry, Cem. Concr. Res. 112 (2018) 96–110, https://doi.org/10.1016/j.cemconres.2018.05.014.
[20] S. Skibicki, M. Kaszyńska, M. Techman, Maturity testing of 3D printing concrete with inert microfiller, MATEC Web Conf. 219 (2018) 3008, https://doi.org/10.1051/matecconf/201821903008.
[21] M. Samy El-Feky, P. Youssef, A. Maher El-Tair, S. Ibrahim, M. Serag, Effect of nano silica addition on enhancing the performance of cement composites reinforced with nano cellulose fibers, AIMS Mater. Sci. 6 (2019) 646–665, https://doi.org/10.3934/matersci.2019.6.646.
[22] G. Ma, L. Wang, A critical review of preparation design and workability measurement of concrete material for largescale 3D printing, Front. Struct. Civ. Eng. 12 (2018) 382–400, https://doi.org/10.1007/s11709-017-0430-x.
[23] Y. Qian, S. Ma, S. Kawashima, G. de Schutter, Rheological characterization of the viscoelastic solid-like properties of fresh cement pastes with nanoclay addition, Theor. Appl. Fract. Mech. 103 (2019), https://doi.org/10.1016/j.tafmec.2019.102262 102262.
[24] A. Kazemian, X. Yuan, E. Cochran, B. Khoshnevis, Cementitious materials for construction-scale 3D printing: laboratory testing of fresh printing mixture, Constr. Build. Mater. 145 (2017) 639–647, https://doi.org/10.1016/j.conbuildmat.2017.04.015.
[25] M. van den Heever, F.A. Bester, P.J. Kruger, G.P.A.G. van Zijl, Effect of Silicon Carbide (SiC) nanoparticles on 3D printability of cement-based materials, Advances in Engineering Materials, Structures and Systems: Innovations, Mecahnics and Applications (2019).
[26] B. Zhu, J. Pan, B. Nematollahi, Z. Zhou, Y. Zhang, J. Sanjayan, Development of 3D printable engineered cementitious composites with ultra-high tensile ductility for digital construction, Mater. Des. 181 (2019), https://doi.org/10.1016/j.matdes.2019.108088 108088.
[27] Y. Zhang, Y. Zhang, G. Liu, Y. Yang, M. Wu, B. Pang, Fresh properties of a novel 3D printing concrete ink, Constr. Build. Mater. 174 (2018) 263–271, https://doi.org/10.1016/j.conbuildmat.2018.04.115.
[28] M. Rubio, M. Sonebi, S. Amziane, 3D Printing of fibre cement-based materials: Fresh and rheological performances, ICBBM2017, 2nd International Conference On Bio-Based Building Materials, Jun 2017, Clermont, Ferrand, France.
[29] S. Cho, J. Kruger, A. van Rooyen, S. Zeranka, G. van Zijl, Rheology of 3D printable lightweight foam concrete incorporating nano-silica, in: V. Mechtcherine, K. Khayat, E. Secrieru (Eds.), Rheology and Processing of Construction Materials, Springer International Publishing, Cham, 2020, pp. 373–381.
[30] S. Cho, J. Kruger, S. Zeranka, A. van Rooyen, G.P.A.G. van Zijl, Mechanical Evaluation of 3D Printable Nano-silica Incorporated Fibre-reinforced Lightweight Foam Concrete, 10th International Conference on Fracture Mechanics of Concrete and Concrete Structures (FraMCoS-X). https://doi.org/10.21012/FC10.232696.
[31] P. Sikora, K. Cendrowski, M. Abd Elrahman, S.-Y. Chung, E. Mijowska, D. Stephan, The effects of seawater on the hydration, microstructure and strength development of Portland cement pastes incorporating colloidal silica, Appl. Nanosci. (2019), https://doi.org/10.1007/s13204-019-00993-8.
[32] Y.W.D. Tay, Y. Qian, M.J. Tan, Printability region for 3D concrete printing using slump and slump flow test, Compos. B 174 (2019), https://doi.org/10.1016/j.compositesb.2019.106968 106968.
[33] S. Skibicki, et al. (2020) Properties of Composite Modified with Limestone Powder for 3D Concrete Printing. In: Bos F., Lucas S., Wolfs R., Salet T. (eds) Second RILEM International Conference on Concrete and Digital Fabrication. DC 2020. RILEM Bookseries, vol 28. Springer, Cham. https://doi.org/10.1007/978-3-030-49916-7_13.
[34] K. Federowicz, M. Kaszyńska, A. Zieliński, M. Hoffmann, Effect of curing methods on shrinkage development in 3d-printed concrete, Materials 13 (11) (2020) 2590, https://doi.org/10.3390/ma13112590.
[35] T. Hirsch, T. Dorn, C. Ehm, D. Stephan, Comparison of Printable Inorganic Binders - Key Properties for 3D Printable Materials. In: Bos F., Lucas S., Wolfs

R., Salet T. (eds) Second RILEM International Conference on Concrete and Digital Fabrication. DC 2020. RILEM Bookseries, vol 28. Springer, Cham., 2020, https://doi.org/10.1007/978-3-030-49916-7_6.
[36] A. Olivas, C.F. Ferraris, N.S. Martys, W.L. George, E.J. Garboczi, B. Toman, Certification of SRM 2493: Standard Reference Mortar for Rheological Measurements, National Institute of Standards and Technology, Gaithersburg, MD, 2017.
[37] M. Liard, L. Oblak, M. Hachim, M. Vachon, D. Lootens, Impact of viscosity on hydration kinetics and setting properties of cementitious materials, Adv. Civil Eng. Mater. 3 (2014) 117–126, https://doi.org/10.1520/ACEM20130096.
[38] O. Ojeda-Farías, P. Hebraud, D. Lootens, M. Liard, J.M. Mendoza-Rangel, Thixotropy of reactive suspensions: The case of cementitious materials, Constr. Build. Mater. 212 (2019) 121–129, https://doi.org/10.1016/j.conbuildmat.2019.03.319.
[39] B.K. Aral, D.M. Kalyon, Effects of temperature and surface roughness on time-dependent development of wall slip in steady torsional flow of concentrated suspensions, J. Rheol. 38 (4) (1994) 957–972, https://doi.org/10.1122/1.550537.
[40] A. Pierre, A. Perrot, A. Histace, S. Gharsalli, E.-H. Kadri, A study on the limitations of a vane rheometer for mineral suspensions using image processing, Rheol. Acta 56 (2017) 351–367, https://doi.org/10.1007/s00397-017-0993-4.
[41] L. Senff, J.A. Labrincha, V.M. Ferreira, D. Hotza, W.L. Repette, Effect of nano-silica on rheology and fresh properties of cement pastes and mortars, Constr. Build. Mater. 23 (2009) 2487–2491, https://doi.org/10.1016/j.conbuildmat.2009.02.005.
[42] V. Meacci, S. Ricci, A. Bruehwiler, D. Lootens, Compact ultrasound board for measurement of concrete compressive strength, in: 2016 IEEE International Ultrasonics Symposium (IUS), Tours, France, IEEE, 18.09.2016 - 21.09.2016, pp. 1–4.
[43] D. Lootens, M. Schumacher, M. Liard, S.Z. Jones, D.P. Bentz, S. Ricci, V. Meacci, Continuous strength measurements of cement pastes and concretes by the ultrasonic wave reflection method, Constr. Build. Mater. 242 (2020), https://doi.org/10.1016/j.conbuildmat.2019.117902 117902.
[44] J. Strzałkowski, H. Garbalińska, Porosimetric, thermal and strength tests of aerated and nonaerated concretes, IOP Conf. Ser.: Mater. Sci. Eng. 245 (2017) 32017, https://doi.org/10.1088/1757-899X/245/3/032017.
[45] A.B. Abell, K.L. Willis, D.A. Lange, Mercury intrusion porosimetry and image analysis of cement-based materials, J. Colloid Interface Sci. 211 (1999) 39–44, https://doi.org/10.1006/jcis.1998.5986.
[46] T.J. Chotard, M.P. Boncoeur-Martel, A. Smith, J.P. Dupuy, C. Gault, Application of X-ray computed tomography to characterise the early hydration of calcium aluminate cement, Cem. Concr. Compos. 25 (2003), https://doi.org/10.1016/S0958-9465(01)00063-4.
[47] S.-Y. Chung, J.-S. Kim, D. Stephan, T.-S. Han, Overview of the use of micro-computed tomography (micro-CT) to investigate the relation between the material characteristics and properties of cement-based materials, Constr. Build. Mater. 229 (2019), https://doi.org/10.1016/j.conbuildmat.2019.116843 116843.
[48] N. Bossa, P. Chaurand, J. Vicente, D. Borschneck, C. Levard, O. Aguerre-Chariol, J. Rose, Micro- and nano-X-ray computed-tomography: a step forward in the characterization of the pore network of a leached cement paste, Cem. Concr. Res. 67 (2015) 138–147, https://doi.org/10.1016/j.cemconres.2014.08.007.
[49] V. Cnudde, A. Cwirzen, B. Masschaele, P.J.S. Jacobs, Porosity and microstructure characterization of building stones and concretes, Eng. Geol. 103 (2009) 76–83, https://doi.org/10.1016/j.enggeo.2008.06.014.
[50] N. Otsu, A threshold selection method from gray-level histograms, Man Cybern. (1979) 62–66.
[51] MATLAB, The MathWorks Inc., Natick, Massachusetts, 2019.
[52] A.M. Gokhale, A. Tewari, H. Garmestani, Constraints on microstructural two-point correlation functions, Scr. Mater. 53 (2005) 989–993, https://doi.org/10.1016/j.scriptamat.2005.06.013.
[53] A. Tewari, A.M. Gokhale, J.E. Spowart, D.B. Miracle, Quantitative characterization of spatial clustering in three-dimensional microstructures using two-point correlation functions, Acta Mater. 52 (2004) 307–319, https://doi.org/10.1016/j.actamat.2003.09.016.
[54] A. Lu, S. Torquato, Lineal-path function for random heterogeneous materials, Phys. Rev. A (1992) 922–929.
[55] S.-Y. Chung, M.A. Elrahman, D. Stephan, P.H. Kamm, Investigation of characteristics and responses of insulating cement paste specimens with Aer solids using X-ray micro-computed tomography, Constr. Build. Mater. 118 (2016) 204–215, https://doi.org/10.1016/j.conbuildmat.2016.04.159.
[56] Y.C. Flores, G.C. Cordeiro, R.D. Toledo Filho, L.M. Tavares, Performance of Portland cement pastes containing nano-silica and different types of silica, Constr. Build. Mater. 146 (2017) 524–530, https://doi.org/10.1016/j.conbuildmat.2017.04.069.
[57] V.V. Potapov, Y.V. Efimenko, D.S. Gorev, Modification of concrete by hydrothermal nanosilica, Nanobuild 11 (2019) 248–265, https://doi.org/10.15828/2075-8545-2019-11-3-248-265.
[58] Z. Xu, Z. Zhou, P. Du, X. Cheng, Effects of nano-silica on hydration properties of tricalcium silicate, Constr. Build. Mater. 125 (2016) 1169–1177, https://doi.org/10.1016/j.conbuildmat.2016.09.003.
[59] J.I. Tobon, O. Mendoza Reales, J.P. Bernabeu, Performance of white Portland cement matrixes blended with nanosilica and limestone for architectural applications, Adv. Cem. Res. (2016) 1600015, https://doi.org/10.1680/jadcr.16.00015.
[60] H.A. Barnes, Thixotropy—a review, J. Nonnewton. Fluid Mech. 70 (1–2) (1997) 1–33, https://doi.org/10.1016/S0377-0257(97)00004-9.
[61] Y. Chen, Y.-F. Deng, M.-Q. Li, Influence of nano-SiO2 on the consistency, setting time, early-age strength, and shrinkage of composite cement pastes, Adv. Mater. Sci. Eng. 2016 (2016) 1–8, https://doi.org/10.1155/2016/5283706.
[62] Y. Qing, Z. Zenan, K. Deyu, C. Rongshen, Influence of nano-SiO2 addition on properties of hardened cement paste as compared with silica fume, Constr. Build. Mater. 21 (2007) 539–545, https://doi.org/10.1016/j.conbuildmat.2005.09.001.
[63] P. Sikora, D. Lootens, M. Liard, D. Stephan, The effects of seawater and nanosilica on the performance of blended cements and composites, Appl Nanosci (2020), https://doi.org/10.1007/s13204-020-01328-8.
[64] G. Land, D. Stephan, The influence of nano-silica on the hydration of ordinary Portland cement, J Mater Sci 47 (2012) 1011–1017, https://doi.org/10.1007/s10853-011-5881-1.
[65] R. Kumar, S. Singh, L.P. Singh, Studies on enhanced thermally stable high strength concrete incorporating silica nanoparticles, Constr. Build. Mater. 153 (2017) 506–513, https://doi.org/10.1016/j.conbuildmat.2017.07.057.
[66] P. Jittabut, Effect of nanosilica on mechanical and thermal properties of cement composites for thermal energy storage materials, Energy Procedia 79 (2015) 10–17, https://doi.org/10.1016/j.egypro.2015.11.454.
[67] D. Kong, X. Du, S. Wei, H. Zhang, Y. Yang, S.P. Shah, Influence of nano-silica agglomeration on microstructure and properties of the hardened cement-based materials, Constr. Build. Mater. 37 (2012) 707–715, https://doi.org/10.1016/j.conbuildmat.2012.08.006.
[68] P.K. Mehta, P.J.M. Monteiro, Concrete: Microstructure, Properties, and Materials, McGraw-Hill, New York, USA, 2006.
[69] A. Stolarska, S. Ciborowski, Sorptive testing of mortars with varying water-cement ratios, E3S Web Conf. 49 (2018) 107, https://doi.org/10.1051/e3sconf/20184900107.
[70] Z. Wu, H. Lian, High Performance Concrete, China Railroad Publishing Company, Beijing, China, 1999.
[71] X. Sun, Y. Hou, Experimental investigation of the macroscopic behavior and microstructure property evolution of hardened cement consolidated tailings, Minerals 10 (2020) 6, https://doi.org/10.3390/min10010006.
[72] I. Netinger Grubeša, B. Marković, M. Vračević, M. Tunkiewicz, I. Szenti, Á. Kukovecz, Pore structure as a response to the freeze/thaw resistance of mortars, Materials (Basel) 12 (2019), https://doi.org/10.3390/ma12193196.
[73] F. Torabian Isfahani, E. Redaelli, F. Lollini, W. Li, L. Bertolini, Effects of nanosilica on compressive strength and durability properties of concrete with different water to binder ratios, Adv. Mater. Sci. Eng. (2016 (2016)) 1–16, https://doi.org/10.1155/2016/8453567.
[74] T.A. Cunha, P. Francinete, M.A. Manzano, L.A. Aidar, J.G. Borges, E.F. Silva, Determination of time zero in high strength concrete containing superabsorbent polymer and nano-silica, J Build Rehabil 1 (2016), https://doi.org/10.1007/s41024-016-0020-7.
[75] G. Quercia, P. Spiesz, G. Hüsken, H.J.H. Brouwers, SCC modification by use of amorphous nano-silica, Cem. Concr. Compos. 45 (2014) 69–81, https://doi.org/10.1016/j.cemconcomp.2013.09.001.
[76] M. Zeidan, M.T. Bassuoni, A. Said, Physical salt attack on concrete incorporating nano-silica, J. Sustainable Cem.-Based Mater. 6 (2017) 195–216, https://doi.org/10.1080/21650373.2016.1218802.
[77] T. Meng, H. Yu, S. Lian, R. Meng, Effect of nano-SiO 2 on properties and microstructure of polymer modified cementitious materials at different temperatures, Struct. Concr. (2019), https://doi.org/10.1002/suco.201900170.
[78] R. Dorey, J. Yeomans, P. Smith, Effect of pore clustering on the mechanical properties of ceramics, J. Eur. Ceram. Soc. (2002) 403–409.
[79] S.-Y. Chung, M. Abd Elrahman, D. Stephan, The effects of anisotropic insulations with different spatial distributions on material properties of mortar specimens, Int. J. Concr. Struct. Mater. 11 (2017) 573–584, https://doi.org/10.1007/s40069-017-0218-3.
[80] S.-Y. Chung, M.A. Elrahman, D. Stephan, Investigation of the effects of anisotropic pores on material properties of insulating concrete using computed tomography and probabilistic methods, Energy Build. 125 (2016) 122–129, https://doi.org/10.1016/j.enbuild.2016.05.006.
[81] R. Cabrillac, Z. Malou, Mechanical modelization of anisotropic porous materials with a homogenization method. Application to aerated concretes, Constr. Build. Mater. (2000) 25–33.
[82] S.-Y. Chung, T.-S. Han, T.S. Yun, K.S. Youm, Evaluation of the anisotropy of the void distribution and the stiffness of lightweight aggregates using CT imaging, Constr. Build. Mater. 48 (2013) 998–1008, https://doi.org/10.1016/j.conbuildmat.2013.07.082.